Journal of Materials Research and Technology 32 (2024) 1062–1073

Contents lists available at ScienceDirect

Journal of Materials Research and Technology

journal homepage: www.elsevier.com/locate/jmrt

High entropy component-induced nanoscale shear banding and twinning enhance Ti6Al4V alloy surface properties

Deyu Jiang [a,1], Yingchen Wang [a,1], Binghao Wang [b,1], Xiaoli Ma [a], Yintao Zhang [a], Vladimir Uglov [c], Weijie Lu [a], Chengliang Yang [b,**], Liqiang Wang [a,*]

[a] *State Key Laboratory of Metal Matrix Composites, School of Materials Science and Engineering, Shanghai Jiao Tong University, Shanghai, 200240, China*
[b] *Guangxi Key Laboratory of Basic and Translational Research of Bone and Joint Degenerative Diseases, Guangxi Biomedical Materials Engineering Research Center for Bone and Joint Degenerative Diseases, Affiliated Hospital of Youjiang Medical University for Nationalities, NO.18, Zhongshan 2nd Road, Baise, Guangxi, 533000, China*
[c] *Belarusian State University, Minsk, 220030, Belarus*

ARTICLE INFO

Handling editor: P Rios

Keywords:
Surface modification
Friction stir processing
High-entropy components
Shear band
Mechanical properties

ABSTRACT

High-entropy alloys (HEAs) present unique advantages in surface modification due to their stable mixed-state structures and resistance to intermetallic compound formation. This study investigates the surface modification behavior of equiatomic TiNbHfZnZr HEA components in Ti6Al4V alloy using friction stir processing (FSP). The aim is to enhance the mechanical properties and structural stability of Ti6Al4V by incorporating HEA elements. It was found that the introduction of high-entropy alloys forms shear bands with distinctive micro and nano gradient structures on the surface of the Ti6Al4V alloy. These shear bands not only significantly refine the grains but also promote β phase and β twin formation. The HEA-induced shear bands enhance the strength and stability of the alloy by creating bcc twins and dislocation networks that suppress martensitic transformation and maintain superelasticity. Concurrently, the introduction of HEA components leads to the formation of stable dual-phase (α + bcc) microstructures within the α matrix, significantly improving hardness and modulus.

1. Introduction

The evolution of materials science has been significantly propelled by the discovery and development of novel alloy systems that can withstand the exigencies of diverse applications, particularly in the realm of aerospace, biomedical implants, and extreme environment engineering. Titanium alloys, and in particular Ti6Al4V, have long been favored for their high strength-to-weight ratio, corrosion resistance, and biocompatibility, making them ideal candidates for applications ranging from aerospace components to orthopedic implants [1–5]. However, the relentless demands of these applications have necessitated the continual enhancement of the alloy's surface properties, particularly in terms of hardness, wear resistance, and fatigue life. Surface modification techniques have emerged as a pivotal strategy to augment the performance of materials without compromising their bulk characteristics [6–10]. Among these, the introduction of nanoscale shear banding and twinning has been shown to significantly enhance the mechanical properties of alloys [11–15]. These nanostructures act as barriers to dislocation motion, thereby increasing the material's strength and ductility. However, the formation of such nanostructures through traditional methods often requires complex and costly processes.

Existing techniques such as chemical etching, physical vapor deposition, and laser surface melting, while improving the surface properties of Ti6Al4V alloys to some extent, still have some limitations. Zhou et al. CoCrMoNbTi alloy coating was fabricated on Ti–6Al–4V substrate by laser cladding technology to produce coating showing BCC solid solution phase [16]. The addition of niobium to the coating results in the formation of a solid solution, which significantly increases its hardness and wear resistance. However, due to the thin coating thickness and the dilution effect of matrix elements, the composition of the area near the matrix is uneven and the hardness is reduced. Ma et al. studied the synergistic effect of Ti and Zr elements in AlCoCrFeNiTi(1-x)Zrx HEA coating of steel, noting that with the increase of Zr content, the structure evolved from double BCC phase to FCC + BCC phase, which led to grain refining, microhardness and wear resistance enhancement [17]. Although excessive Zr content can lead to defects, reduced corrosion and

---

* Corresponding author.
** Corresponding author.
E-mail addresses: stbyyl@126.com (C. Yang), wang_liqiang@sjtu.edu.cn (L. Wang).
[1] These authors contributed equally to this work.

https://doi.org/10.1016/j.jmrt.2024.07.225
Received 17 June 2024; Received in revised form 25 July 2024; Accepted 29 July 2024

oxidation resistance. Friction stir processing (FSP) is a solid-state processing technique known for its ability to refine grain structures and induce phase transformations in various alloys [18–23]. By using the friction stirring process, the production process of nano-composites on the surface of metal materials with particle-reinforced materials is effectively realized. This approach has been shown to be successful in creating highly functional materials with desired properties [24–28]. FSP technology, by its very nature, is capable of producing a fine-grained microstructure in the metal matrix [29–32]. Additionally, the incorporation of reinforcement particles into the matrix further refines the microstructure and enhances the surface properties of the final product [33–36]. However, the commonly used reinforcement is mainly ceramic, which makes the surface poor in toughness despite high hardness [37–42].

High entropy alloys (HEAs) have been demonstrated to possess a range of unique properties, including high strength, excellent ductility, and superior resistance to deformation due to their sluggish diffusion kinetics and the formation of solid solutions [43–46]. The introduction of high entropy components (HECs) into traditional alloys presents a novel avenue for the formation of nanoscale shear bands and twins, potentially offering a simple and effective means to enhance the surface properties of alloys such as Ti6Al4V [47–50]. The incorporation of HECs into Ti6Al4V via FSP is a groundbreaking approach that harnesses the unique characteristics of HEAs to induce nanoscale shear banding and twinning at the alloy's surface [51,52]. Elements with excellent biocompatibility such as Ti, Nb, Hf, Zr, and Zn have been widely used in the development of bio-high entropy alloys [53–55]. Consequently, these bio-high entropy components are well-suited for use as surface modification layers. However, the potential of FSP to systematically introduce HECs and investigate the resulting nanoscale shear banding and twinning phenomena has been largely unexplored.

To bridge this gap, it is imperative to examine the effects of HEC-induced nanoscale shear banding and twinning on the surface properties of Ti6Al4V alloy [56,57]. Our findings reveal that the introduction of HECs via FSP not only refines the microstructure but also induces the formation of a complex network of nanoscale shear bands and twins at the surface. These nanostructures act as efficient barriers to dislocation movement, thereby significantly enhancing the alloy's strength and hardness. Furthermore, the high-entropy components contribute to the stabilization of a unique dual-phase microstructure, which further augments the material's resistance to deformation and wear.

This study presents a comprehensive investigation into the surface modification behavior of Ti6Al4V alloy induced by high-entropy components. The results highlight the synergistic effects of nanoscale shear banding and twinning on the mechanical properties of the alloy, offering a novel strategy for the design and fabrication of advanced materials with superior performance for critical applications where surface properties are paramount.

2. Experimental methods

2.1. Preparation of samples

The rolled Ti6Al4V plate, with a thickness of 5 mm, was processed via FSP using a W–Re alloy tool in an argon atmosphere. Prior to processing, a groove measuring 1 mm in width and 0.5 mm in depth was machined along the FSP direction on the sample surface. Equiatomic TiNbHfZnZr powders, with a particle size of 50 nm, were mixed for 4 h using a YXQM-4L planetary ball mill, at a powder weight ratio of 5:1 and a rounding speed of 200 rpm. The mixed powder was then placed into the pre-cut groove. Previous research has demonstrated that the rotational speed of the FSP stirring probe directly affects the microstructure and performance. The two main processing parameters in FSP, namely the rotational speed and the number of passes, have a significant effect on the microstructure of the machined material. Due to the severe plastic deformation and severe stirring effect experienced in the stirred zone, increasing the number of passes during the FSP process can fine the grains, thus significantly optimizing the surface properties. In light of our previous research, we selected the stirring probe speeds of 375 rpm and 225 rpm [58–60]. The FSP was conducted with a probe diameter of 12 mm and a probe plunge depth of 1.7 mm, at rotation speeds of 375 rpm and 225 rpm, and a travel speed of 50 mm/min. During the process, the powders were effectively dispersed and made full contact with the matrix. Only one pass was performed to prevent the powder from spilling. The schematic of this process is depicted in Fig. 1.

Referring to our previous studies and existing literature reports, heat treatment at high temperature (600 °C) for half an hour is required for further diffusion and homogenization of high-entropy alloying elements. Subsequent to FSP, heat treatment was applied at 600 °C for either 30 min or 3 h to promote further diffusion of the added elements. The various specimens subjected to different FSP durations are detailed in Table 1.

2.2. Microstructural observations

The microstructure of the FSPed specimen was characterized using optical microscopy (OM), scanning electron microscopy (SEM, FEI Nova 400), and transmission electron microscopy (TEM, JEOL JEM-2100EX, 200 kV). SEM specimens were prepared by cutting the material into pieces of 10 mm × 10 mm x 5 mm. These pieces were then ground up to 3000# grit and polished before being etched in a mixed acid solution (HF:HNO3:H2O = 1:3:10 by volume) for 10 s. TEM specimens were thinned to a thickness of 50 μm and then punched into 3 mm diameter disks. These disks underwent twin-jet electropolishing in a mixed acid alcohol solution (HClO4:CH3OH:C4H9OH = 6:64:30 by volume) at 35 V and −40 °C.

2.3. Nanoindentation tests

Nanoindentation tests were carried out using a NANO Indenter G200 Tester, which employs a lock-in technique to determine indentation depth-dependent mechanical properties at the same position on the sample during a single loading-unloading cycle. The indentation depth was limited to 2000 nm. The loading rate was maintained at 1 mN/s, with a holding time of 5 s at the maximum depth. To minimize the influence of the stress field, indentations were spaced 30 μm apart. Measurements were taken 100 μm from the processed surface.

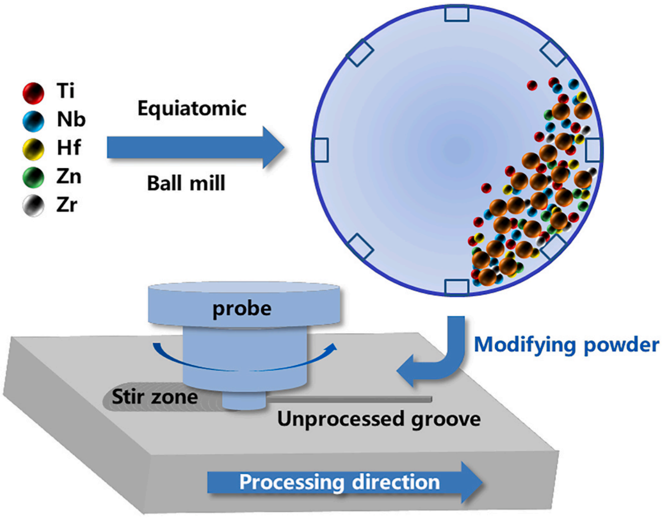

Fig. 1. Schematic diagram of the friction stir process with modification of high-entropy components.

Table 1
Rotation rate and corresponding specimen.

Specimen name	Rotation rate	Heat treatment
375	375 rpm	/
375_{HT1}	375 rpm	600 °C/30 min
375_{HT2}	375 rpm	600 °C/3 h
225	225 rpm	/
225_{HT1}	225 rpm	600 °C/30 min
225_{HT2}	225 rpm	600 °C/3 h
TC4	225 rpm	/

3. Results

The OM and SEM images of the specimens without heat treatment are displayed in Figs. 2 and 3. In Specimen 375, an 800 μm deep stir zone is observed, characterized by equiaxed grains. Distinct stripes are visible near the deformed surface, while only faint stripes are noticeable in the deeper regions. Both the dark and fuzzy fringes have an almost equal atomic TiNbHfZnZr composition, corresponding to a high entropy component. In contrast, Specimen 225 also exhibits an 800 μm deep stir zone, but the stripes are confined to the near-surface area. Notably, no faint stripes are detected in the deeper regions. Additionally, equiaxed grains are present only in the near-surface region, unlike in the deeper part of the stir zone. The differences in stripe distribution and grain structure between Specimen 375 and Specimen 225 suggest incomplete element diffusion and recrystallization in Specimen 225 [61,62]. This observation highlights the variability in microstructural evolution depending on the processing parameters.

To further investigate the stripes composed of high-entropy components, TEM analysis was conducted. Fig. 4a reveals several parallel dark shear bands within the α matrix. These bands are less than 1 μm in length and under 100 nm in width, with non-uniform spacing between them. The region between adjacent shear bands contains a lower density of dislocations (Fig. 4b), while the area between separated bands exhibits a distinct dislocation network (Fig. 4d). Notably, even isolated shear bands do not show dislocation networks near them. The dislocations surrounding these bands are oriented perpendicular to the shear band boundary, which demarcates the shear band from the distant dislocation network. Furthermore, these perpendicular dislocations extend into the interior of the dislocation network, indicating interactions between different regions [63].

The diffraction spot analysis, shown in Fig. 4c, indicates that the dark shear bands are primarily composed of the bcc phase. However, the short length and distribution of these bands within the α grains suggest that they are not the typical β phase. In contrast, Fig. 4e depicts deformed α grains without shear bands, with diffraction patterns (Fig. 4f) showing only the α phase and no bcc phase. In these grains, the dislocation network fills the interior, and no areas of unidirectional dislocations are found. This difference highlights that the distribution of dislocations is related to the presence of shear bands.

In Fig. 5a, an incomplete shear band is observed. Restricted by the phase boundary, this band extends across the α phase and measures approximately 300 nm in length. Within the shear band, parallel acicular needles emerge from the phase boundaries and extend across the band. These needles vary in width, and their ends are indistinct. The diffraction pattern of the shear band, shown in Fig. 5b, reveals spots corresponding to different bcc lattices, but no bright line is observed. This indicates that the lattice in this region is metastable due to the presence of various bcc-stable elements, and the structure is not a result of stacking faults [64,65].

Fig. 6 illustrates the internal structure of a fully formed shear band. Perpendicular stacking faults are found outside the shear band, while acicular structures are present inside it. However, the substructure varies in form. According to the Fast Fourier Transform (FFT) in Fig. 6c, the shear band comprises both α and bcc phases. A distinct boundary between the α phase of the matrix and the α phase within the shear band suggests that the α phase in the shear band and the bcc phase together form a unique dual-phase structure [66–68]. The angle between the growth direction of the bcc needles and the shear band boundary is 33°. The lengths of the bcc needles differ, and a twin structure is evident in the larger needles, indicating the asynchronous formation of needles and twins [69].

Outside the shear band, stacking faults are connected to the α phase rather than to the bcc needles within the shear band, highlighting a special relationship between phase distribution and stacking faults. In Fig. 6d, bcc acicular needles traverse the shear band and form clear twin structures. The varying thicknesses on both sides of the twin boundary indicate heterogeneously distributed nucleation sites for the twins. Notably, no α phase is observed in this shear band, suggesting a higher concentration of bcc-stable elements within the shear band, as depicted

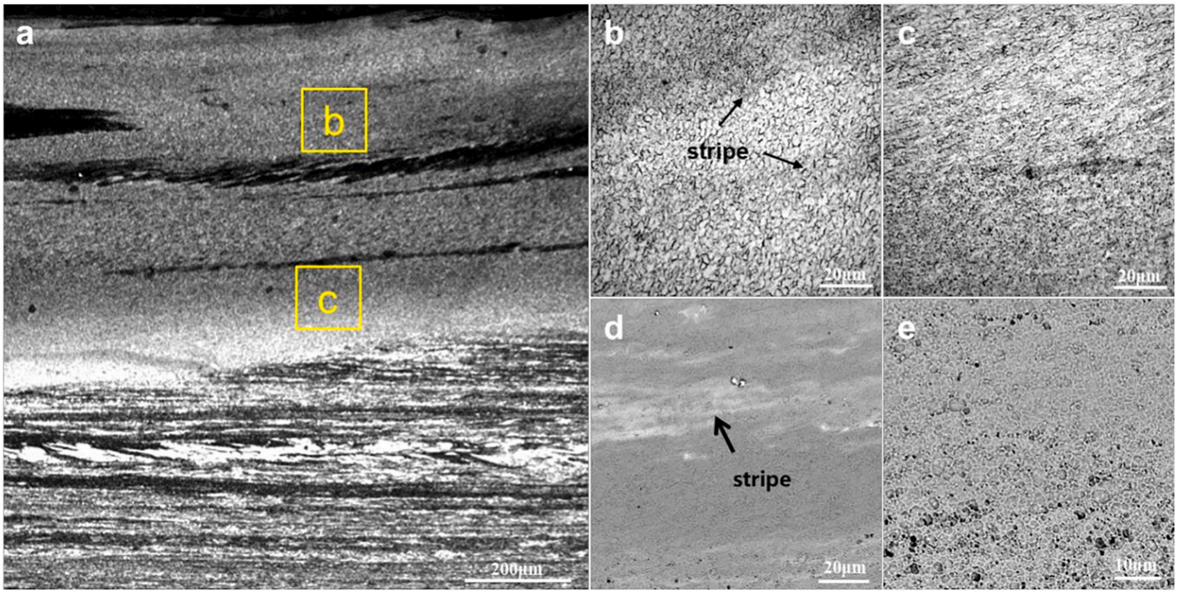

Fig. 2. Microstructure of Specimen 375: (a) OM image of the stir zone; (b) OM image of the shallow stir zone at higher magnification; (c) OM image of the deep stir zone at higher magnification; (d) SEM image of the shallow stir zone; and (e) SEM image of the deep stir zone.

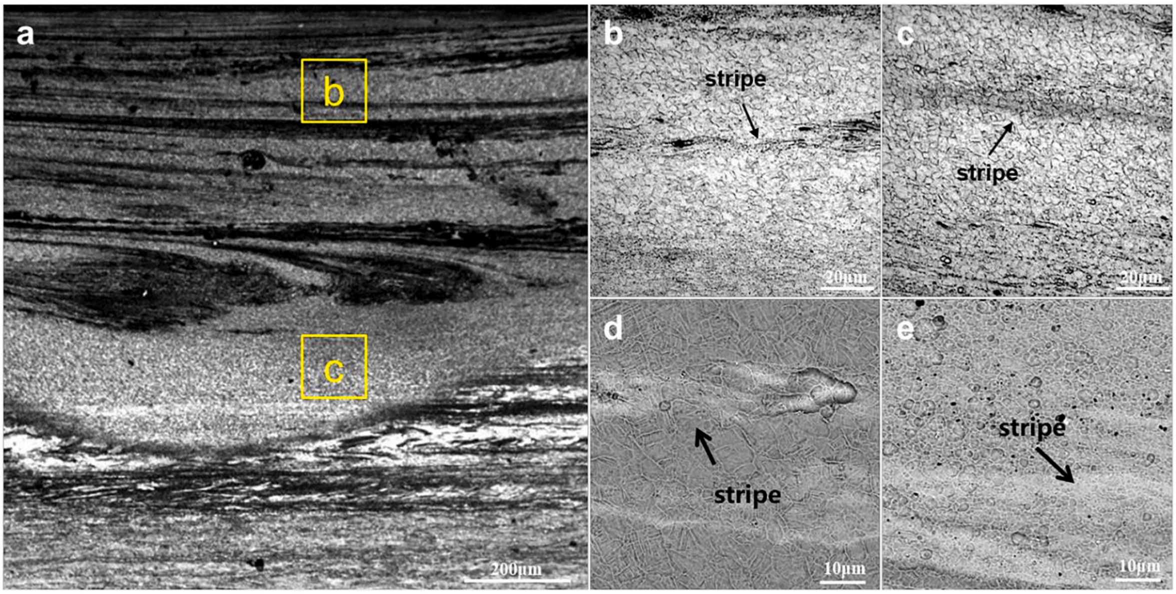

Fig. 3. Microstructure of Specimen 225: (a) OM image of the stir zone; (b) OM image of the shallow stir zone at higher magnification; (c) OM image of the deep stir zone at higher magnification; (d) SEM image of the shallow stir zone; and (e) SEM image of the deep stir zone.

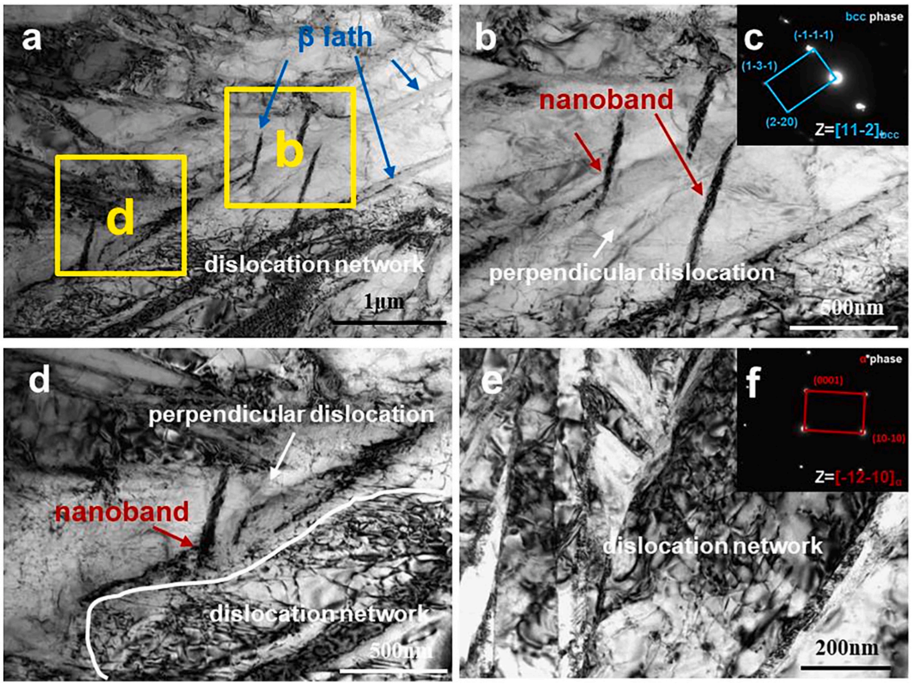

Fig. 4. TEM images of the stir zone of Specimen 375: (a) bright field image of a stripe composed of high-entropy components; (b, d) images of nanoscale shear bands and surrounding regions at higher magnification; (c) diffraction pattern of the nanoscale shear band in (b); (e) image of a deformed α grain without a nanoscale shear band; and (f) diffraction pattern in (e).

in Fig. 6d [70].

The structural configuration at the junction of the shear band and the β phase is illustrated in Fig. 7. It can be observed that no bcc needle is directly connected to the β phase; instead, the α phase serves as an intermediary. This arrangement suggests a high-stress level in the shear band [71]. Additionally, a stacking fault is observed at the connection point, which positively influences shear band formation [72]. Diffraction analysis in Fig. 7c confirms the presence of α and β phases near the connecting position. In comparison to the results presented in Fig. 7d, the lattice constant of the bcc phase within the shear band is observed to be larger than that of the typical β phase. This indicates a distinct elemental composition between the β phase and bcc needles. Moreover, no significant change in the lattice constant of the α phase is observed. The stability of the α phase lattice constant suggests that modifying elements primarily affect the bcc phase structure.

The shear band near the α twin is shown in Fig. 8a. This shear band is smaller, approximately 100 nm in length, compared to those in Fig. 6. The high-resolution image in Fig. 8b reveals a bcc twin structure within the shear band, with no α phase present in this region. The boundary of the bcc twin extends from the α twin boundary, indicating that the bcc twin originates from the α twin. Unlike the results in Fig. 6, the bcc twin boundary in this shear band is parallel to the phase boundary rather than

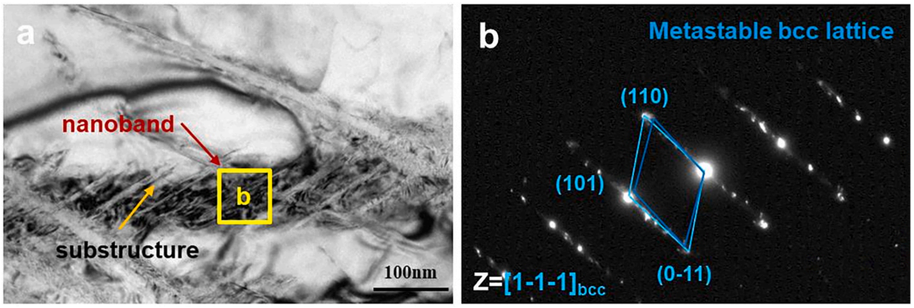

Fig. 5. TEM images of incompletely formed nanoscale shear bands with substructures: (a) bright-field image and (b) diffraction patterns of the nanoscale shear band in (a).

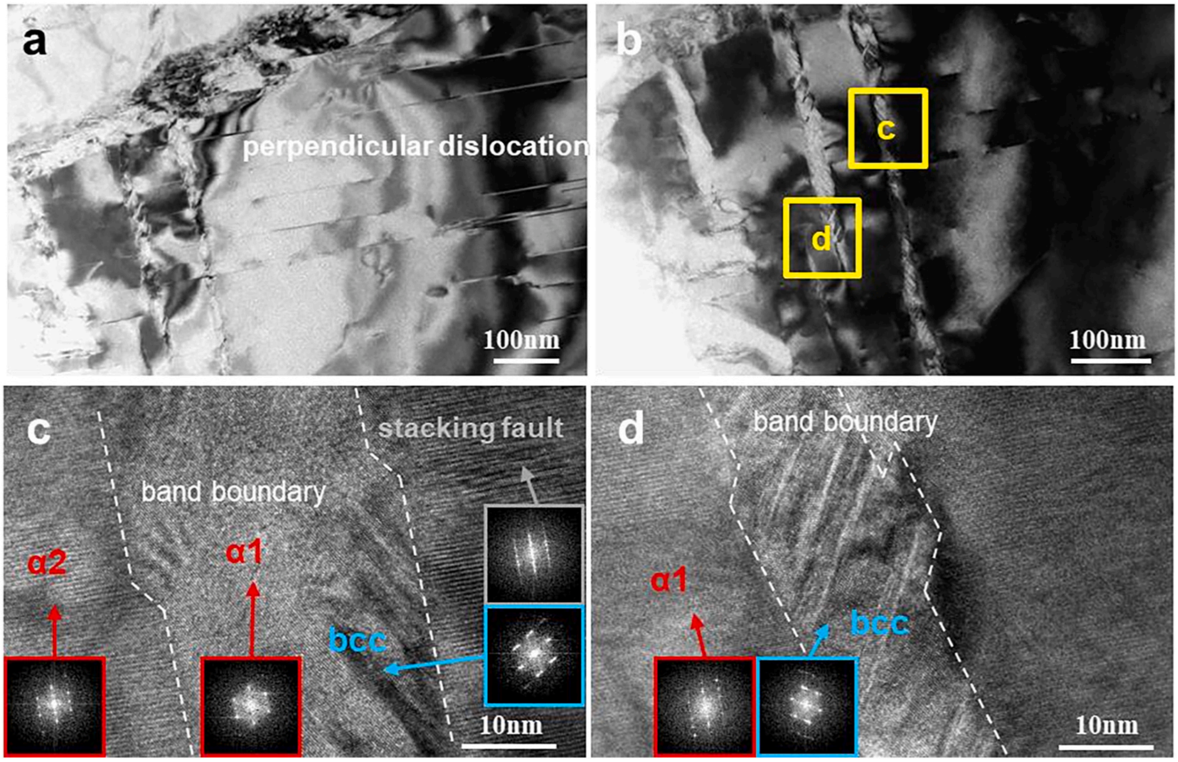

Fig. 6. TEM images of complete shear bands with substructures in the stir zone of Specimen 375:(a) bright-field image; (b) bright-field image at higher magnification; (c–d) high-resolution images of the shear bands in (b).

at an angle of 33°. Vague characteristics near the twin boundary suggest an incompletely transformed stacking fault structure [73]. In addition to the twin boundary in the central area, a twin structure is also observed near the phase boundary. These outer twins are approximately three atomic layers thick and exhibit distinct twin boundaries.

Along the bcc band, no stacking faults are observed in the surrounding α grains, similar to the findings in Fig. 6. One side of the band is connected to the α twin, while the other side shows a vague phase boundary, indicating the growth direction of the bcc twins [74]. Furthermore, shear bands composed of α and bcc phases are found nearby. The coexistence of these two types of bands and their similar short lengths (100 nm) reflect the fragmentation of the bcc bands. Bcc-stable elements diffuse in different directions when they encounter the twin structure of the matrix. As a result, the content of bcc-stable elements decreases in one direction, leading to a reduction in the length of the bands.

The mechanical properties are shown in Fig. 9. As shown in Fig. 9a, concerning a given load−displacement curve, necessary parameters are achieved, unloading (h_r), elastic recovery (h_{er}) and superelastic recovery (h_{sr}). h_{er} and h_{sr} are determined by tangent and vertical lines from the end of the upper platform, respectively. To calculate the values of the modulus and hardness, the contact depth (h_c) and contact area (A_c) need to be obtained in advance:

$$h_c = (h_{er} + h_{sr} + h_r) - \epsilon\left(\frac{P_m}{S}\right) \tag{1}$$

$$A_c = 24.56h_c^2 + 793h_c + 4238\sqrt{h_c} \tag{2}$$

For the pyramidal indenter, ε is 0.75. The reduced modulus (E_r) and modulus (E) are then determined by:

$$E_r = \frac{\sqrt{\pi}}{2} \times \frac{S}{\sqrt{A_c}} \tag{3}$$

$$\frac{1}{E_r} = \frac{1-\nu^2}{E} + \frac{1-\nu_i^2}{E_i} \tag{4}$$

v (0.34) is Poisson's ratio of TC4. E_i (1140 GPa) and v_i (0.07) are the

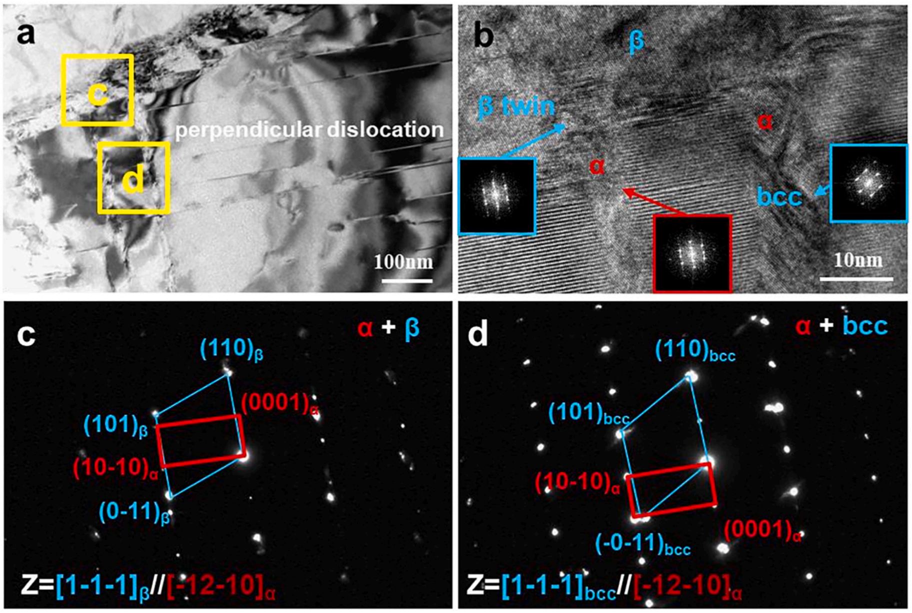

Fig. 7. TEM images of shear bands with substructures in the stir zone of Specimen 375: (a) bright-field image; (b) image of the connecting region at higher magnification; (c) diffraction patterns of theconnecting region in (a); (d) diffraction patterns of the shear bands and surrounding region in the α matrix.

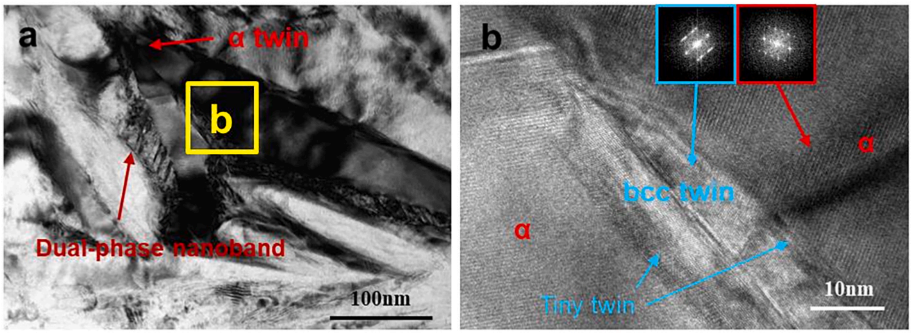

Fig. 8. TEM images of the shear band near the α twin and the surrounding region: (a) bright field image and (b) high-resolution image of the shear band near the α twin in (a).

modulus and Poisson's ratio of the indenter, respectively. The hardness value (H) can be calculated as follows:

$$H = \frac{P_m}{A_c} \tag{5}$$

Finally, the superelastic strain recovery η_{sr}, which measures the superelasticity of the specimen, is obtained by:

$$\eta_{sr} = \frac{h_{sr}}{(h_{er} + h_{sr} + h_r)} \tag{6}$$

A detailed comparison of the modulus and hardness among the specimens is shown in Fig. 9b. Specimens processed at a high rotation rate (375 rpm) exhibit a typical softening phenomenon during heat treatment. The modulus decreases from 109.5 GPa to 102.6 GPa, and the hardness decreases from 4.43 GPa to 3.88 GPa. These similar decreases in modulus and hardness indicate that no significant reaction or diffusion of high-entropy components occurs during heat treatment. Recovery softening appears to be the main mechanism during heat treatment [80]. In contrast, specimens processed at a moderate rotation rate (225 rpm) display an atypical softening phenomenon. The modulus initially increases from 109.0 GPa to a peak value of 113.0 GPa, before rapidly decreasing to 101.8 GPa. The hardness remains stable at 4.39 GPa during the first 30 min, then decreases rapidly to 3.85 GPa over the next 2.5 h. The different trends in mechanical properties compared to those processed at a higher rotation rate suggest that the diffusion of high-entropy components is incomplete. Heat treatment promotes further diffusion and reactions of high-entropy components [81].

The initial increase in modulus and stable hardness during the first 30 min can be attributed to a combination of high-entropy component strengthening and recovery softening. Compared to the FSPed TC4 specimen without additional modifying elements (modulus of 101.2 GPa and hardness of 4.00 GPa), the high-entropy element-modified specimens show significant strengthening effects and maintain advantages during short heat treatments. This indicates the relative stability of the microstructure induced by high-entropy components. Moreover, the modified specimens generally retain the high hardness and low modulus characteristics of the TC4 alloy (Fig. 9c), which are essential for medical implant applications. The statistics of superelastic strain recovery are displayed in Fig. 9d. Despite varying rotation rates and heat treatment durations, the values of superelastic strain recovery are similar. This stability in superelasticity suggests that the effects of heat treatment and diffusion of high-entropy components on martensitic transformation are negligible.

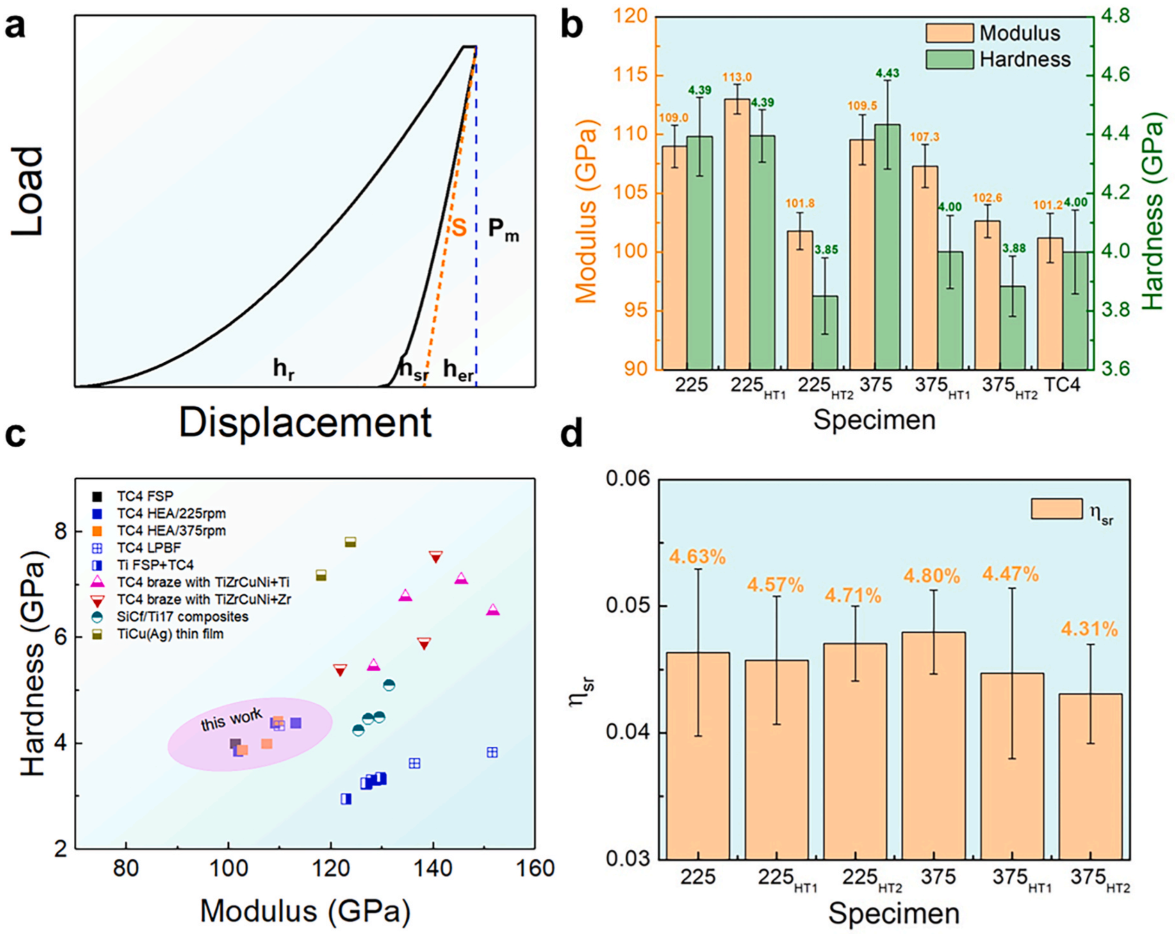

Fig. 9. Nanoindentation results for the modified specimens: (a) schematic diagram of the nanoindentation curve; (b) detailed comparison of the modulus and hardness among the specimens in Table 1; (c) comparison of the modulus versus hardness calculation results for the FSPed TC4 alloy and previously reported modified Ti alloys [75–79]; (d) superelastic strain recovery rates of the specimens in Table 1.

4. Discussion

4.1. Formation of high-entropy nanoscale shear bands

4.1.1. Stability of the high-entropy dual-phase structure

Compared to bulk high-entropy alloys, high-entropy component-modified alloys exhibit different elemental compositions, which affect the high entropy characteristics and resulting structure. In this study, the bcc phase induced by high-entropy components is primarily distributed within the α matrix. Consequently, the change in elemental composition is reflected by the dilution of Ti and Al. According to Pavel Kovacocy's findings, the atomic ratio of Ti to Al is approximately 0.874:0.126 [82]. Various empirical formulas and phase formation criteria based on thermodynamic physical characteristics have been published and widely applied to analyze the microstructure of HEAs [83]. The atomic size mismatch (δr) can be calculated as follows [84]:

$$\bar{r} = \sum_{i=1}^{n} c_i r_i \tag{7}$$

$$\delta r = \sqrt{\sum_{i=1}^{n} c_i \left(1 - \frac{r_i}{\bar{r}}\right)^2} \tag{8}$$

where c_i and r_i are the atomic fraction and the atomic radius of the ith element, respectively. $\bar{r}$ is the average atomic radius, and n is the number of principal components. The radius of the critical elements are listed in Table 2.

Table 2
Radius of the elements.

element	Ti	Nb	Hf	Zn	Zr	Al
Radius (pm)	146	143	158	140	160	143

For the equiatomic TiNbHfZnZr alloy, the average atomic radius ($\bar{r}$) is 149.4 p.m., which corresponds to a larger lattice constant as confirmed by diffraction analysis shown in Fig. 7. The atomic size mismatch (δr) is 5.41%, which exceeds the 4.3% threshold typically associated with a dual-phase microstructure [85,86]. It is reasonable to infer that the dual-phase microstructure of the TiNbHfZnZr system consists of bcc and hcp phases.

As the dilution of Ti and Al continues, the changes in the average atomic radius and atomic size mismatch are illustrated in Fig. 10a and b. Compared with the β phase, which is primarily composed of Ti atoms, the high-entropy bcc phase maintains a larger lattice constant during element diffusion. Initially, the atomic size mismatch decreases slowly. However, the rate of decrease becomes significant as the total content of Nb, Hf, Zn, and Zr drops below 50%. Consequently, the dual-phase structure rapidly transitions into an hcp structure after reaching a certain degree of dilution. Under these conditions, the dual-phase shear band tends to dissolve directly into the α matrix rather than separating into high-entropy nanoparticles. This observation aligns with the small quantity of nanoparticles shown in Figs. 2 and 3.

Moreover, the presence of high-entropy stripes at different depths (Figs. 2 and 3) indicates that the dilution of the α matrix is not entirely

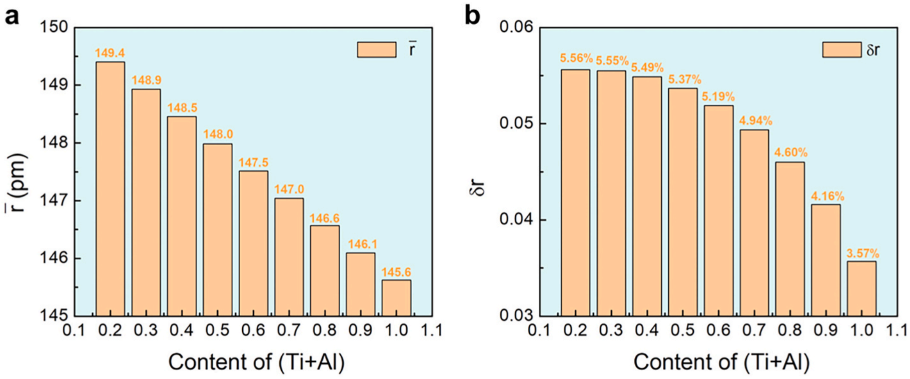

Fig. 10. Stability of the high-entropy region as dilution of the α matrix proceeds: (a) average atomic radius; (b) atomic size mismatch.

uniform. Some stripes dissolve first, while other regions retain the dual-phase structure. During subsequent heat treatment, no additional deformation occurs, and the dilution process continues at a slower rate compared to the initial FSP. As a result, the shear band stabilizes, and heat treatment can be used to further enhance the degree of the high-entropy structure.

4.1.2. Diffusion of high-entropy components

As shown in Figs. 2a and 3a, in addition to the stripe regions, high-entropy components also exist as particles. The presence of these two forms indicates the diffusion of high-entropy components. During FSP, the aggregation of powder is suppressed, and high-entropy components are distributed over a larger region near the Ti alloy surface. There are two primary diffusion routes for these components.

The first route involves the initial β phase of the Ti alloy. Due to the bcc structure of the β phase, the addition of bcc-stable elements leads to lattice distortion, forming a solid solution with high stress concentration. However, diffraction analysis revealed the typical lattice of the β phase in the FSPed Ti alloy, suggesting that most high-entropy components are distributed away from the β phase, influenced by sluggish diffusion.

The second route is distribution within the α matrix. The α matrix has an hcp structure, different from the high-entropy component-induced phase, resulting in the formation of a new phase boundary. Defects and stresses tend to localize at these phase boundaries, and new phases induced by high-entropy components are minimally affected by the α matrix [87]. Thus, the lattice of the new phase is primarily determined by the diffused bcc-stable elements. According to Fig. 5, diffusion of high-entropy elements occurs in two stages on different scales. The first stage involves diffusion into the α matrix, leading to the formation of nanoscale shear bands. Different diffusion rates of each element cause a heterogeneous distribution, resulting in the separate formation of bcc needles with varying lattice constants [88]. The second stage involves diffusion among the high-entropy components, leading to a uniform distribution within the shear band and the transformation of the metastable bcc lattice into a stable structure, as shown in Fig. 7d.

4.1.3. Growth of the shear band and surrounding nanostructure

In the FSP-treated TC4 alloy, β laths, dislocations, and twins are the primary nanostructures in the stir zone. The length of the shear band is determined by the spacing between the β laths. As shown in Fig. 4, β laths with different spacings are observed. Shear bands connect adjacent β laths rather than crossing them. The start and end points of these shear bands are within the β laths rather than at their boundaries. In Fig. 7, bcc needles induced by high-entropy components are distributed outside the β lath, while the band extends into the β lath and connects to β twins. These β twins are induced by increased stress from lattice distortion. In regions away from the shear bands, stress remains low, and β twins are not observed. Thus, the length of β twins is limited by the width of the shear bands, extending the β twins into the shear bands. Due to uneven stress distribution, β twin-induced shear bands exhibit different thicknesses, corresponding to different depths of shear bands extending into the β laths. The β twin boundary is parallel to $(112)_\beta$ and $(0001)_\alpha$ but not to $(112)_{bcc}$. Therefore, the generation of twins induced by high-entropy components is obstructed near the β phase, necessitating the α phase as a connecting area.

Moreover, the shear bands in Fig. 4, which have similar widths but different lengths, indicate that the width of the shear band is influenced primarily by the diffusion of high-entropy components rather than by β laths. During FSP, the movement of dislocations to the high-entropy region is continuous. As shown in Figs. 6 and 7, shear bands are obstructed by β twins and connect to stacking faults in the α matrix [89, 90]. Both twins and stacking faults can absorb and hinder dislocations. Given the high temperature during FSP, some dislocation blockage is relieved, making dislocation absorption the primary mechanism near stacking faults. During shear band formation, dislocations contribute to the formation of stacking faults in both the β phase and the α matrix. Dislocation movement is easier in the bcc structure than in the hcp structure, causing stacking faults in the β phase to absorb dislocations and transform into wider twins. In contrast, stacking faults in the α matrix are less likely to develop. During deformation, dislocations move to shear band boundaries and are partially absorbed in the $(10\text{-}10)_\alpha$ plane. Movement in the $<0001>_\alpha$ direction is difficult, so remaining dislocations form initial stacking faults in the α matrix. Several close stacking faults form nearly simultaneously, each with a limited source of dislocation, resulting in narrower stacking faults early on. No heterogeneous particles are observed between stacking faults to generate new dislocations, so the development of stacking faults relies on dislocations outside the affected region. However, dislocation movement to shear bands is blocked by stacking faults, and dislocation absorption in the $(10\text{-}10)_\alpha$ plane cannot be achieved. These dislocations subsequently entangle and form dislocation networks, suppressing the development of stacking faults and eventually stopping the process. Additionally, the migration of the shear band boundary parallel to the bcc twin boundary occurs only over a small distance, indicating a stable width of the shear band. As shown in Fig. 6, the shear band boundary is nearly straight, confirming limited migration.

4.2. Evolution of the substructure in the shear band

4.2.1. Nanotwinning in the shear band across the α matrix

The formation of substructures within the shear band is a complex process influenced by stacking faults and the content of high-entropy components. After the shear band forms, bcc-stable elements tend to further aggregate, forming the bcc phase. Meanwhile, the remaining elements aggregate to form an α phase within the shear band. Although an identical α lattice is observed in both the shear band and the α matrix, the α phase in different regions exhibits mismatches indicative of stacking faults.

As shown in Fig. 6c, the close-packed $(0001)_\alpha$ plane is staggered and perpendicular to the shear band boundary, while the (10-10)α plane is parallel to it. The lowest surface energy of the $(0001)_\alpha$ plane determines the primary type of stacking fault. The similarity in the α lattice results in stacking faults directly connecting to the α phase rather than the bcc phase within the shear band. Under these conditions, the shear band boundary between stacking faults, where stress is concentrated, serves as an ideal nucleation site for bcc needles. All bcc needles grow at an angle of 33° from the boundary, a direction parallel to $(112)_{bcc}$ and $(10–11)_\alpha$. Due to differences in interplanar spacings of $(112)_{bcc}$ and $(10–11)_\alpha$, the bcc phase tends to form thin structures to minimize lattice distortion in the shear band [91,92].

Furthermore, an incomplete twin structure is observed near the shear band boundary, with the twin boundary parallel to $(112)_{bcc}$, consistent with the bcc needle tip. The twinning process occurs concurrently with the growth of the bcc phase, aiding in stress reduction [93]. As the content of bcc-stable elements increases in the shear band, the newly formed bcc structure thickens and eventually occupies the entire shear band. The twinning process follows suit, with the twin becoming the dominant structure. Bcc needles of varying lengths indicate that the bcc growth process is asynchronous. As the bcc phase continuously generates and grows, newly formed bcc structures contact and compress previously formed bcc phases. To alleviate internal stress, twinning occurs at the contact points near the bcc generation boundary, while the opposite side is less affected, forming an acicular structure with one fine and one thick tip. As shown in Fig. 6d, thin acicular tips are on the left, while thicker tips are on the right. The uniform orientation of the acicular structure suggests that the bcc phase is generated at only one shear band boundary. This inconsistency results from significant stress concentration at the nucleating boundary. The right boundary of the shear band is significantly influenced by dislocation absorption, exhibiting a twisted shape, while the left side remains relatively straight.

In the shear band, the spacing between bcc needles is determined by their density, corresponding to the content of high-entropy components. When the entropy content is low, as in Fig. 6c, the spacing between bcc needles is large, allowing lattice distortion to be easily relieved. According to Mu et al., stacking faults can generate and grow in new directions between previously formed stacking faults [94]. As shown in Fig. 7b, twins form in two directions corresponding to $(112)_{bcc}$. The amounts and thicknesses of twins in each direction differ significantly, indicating asynchronous twin generation due to the limited diffusion speed of high-entropy components. During shear band formation and substructure development, the diffusion of bcc-stable elements is incomplete. Following the initial formation of twins, remaining bcc-stable elements continue to form additional twins, resulting in thinner twins in the second stage due to lower remaining bcc-stable element content. Under these conditions, bcc-stable elements with high content tend to distribute along the shear band boundary, with no preferential twin generation position observed, differing from Fig. 6c.

4.2.2. *Influence of the α twin on nanotwinning in the shear band*

The α twin also affects shear band formation. Since the twinning process in the α matrix occurs without element diffusion during FSP, the α twin forms earlier than the shear band. Due to lattice distortion and higher stress, the twin boundary becomes the nucleation site for surrounding high-entropy components. As shown in Fig. 8b, a new bcc phase forms on both sides of the twin boundary. Considering the mismatch between the bcc and α phases, additional lattice distortion occurs, making the twin boundary an irregular elongated area with several layers of twins. Dislocation accumulation occurs near the connection area between the α twin and bcc phases, forming a small bcc twin at the boundary. The bcc twin boundary is parallel to $(112)_{bcc}$ and $(10–11)_\alpha$, consistent with Fig. 6, confirming the bcc twin's preferential orientation unaffected by size or shape. Furthermore, the bcc twin boundary is also parallel to the α twin boundary.

As the bcc twinning process continues, high-entropy components tend to diffuse along the initial α twin boundary, forming a bcc lattice. Consequently, a bcc twin connected by an α twin displays a complete lath rather than several needles. However, the growth of bcc twins is restricted by the sluggish diffusion of high-entropy components. As shown in Fig. 8a, surrounding bcc-stable elements can form additional shear bands before the bcc laths reach longer lengths. Without sufficient element sources, the bcc lath is shorter than typical shear bands. The different twinning processes in the shear bands are illustrated in Fig. 11.

4.3. *Influence of the modified microstructure on mechanical properties*

Shear bands induced by high-entropy components play a crucial role in modifying mechanical properties, rather than acting as isolated reinforcement. These bands, along with β twins at their ends, stacking faults perpendicular to the shear band boundaries, and surrounding dislocation networks, develop extensive nanoscale regions that significantly affect the surface area and result in notable modifications.

4.3.1. *Strengthening effect of shear bands and dislocations*

According to K. Tsai et al., the high interaction energy of high-entropy elements leads to sluggish diffusion, necessitating higher thermal energy to break up metallic bonds in HEAs compared to conventional alloys [43]. Resistance to shear localization in HEAs is promoted but difficult to further develop [95]. As illustrated in Fig. 6, bcc twins induced by high-entropy elements occupy the majority of the shear band. The shear band boundary struggles to move parallel to $(112)_{bcc}$, maintaining the shear band's size stability post-FSP. Consequently, shearing deformation is minimal after FSP, with the strengthening effect predominating over softening.

Strengthening effects arise from two factors in different regions. The first factor is nanotwinning within the shear band. Deformation twinning, by continuously introducing new interfaces and reducing the mean free path of dislocations during deformation, leads to significant work hardening [96]. As shown in Fig. 5a, incomplete diffusion of high-entropy elements post-FSP allows twinning to continue during subsequent deformation. Newly generated dislocations are blocked and absorbed by twins and shear band boundaries, causing lattice distortion (shown in Fig. 6) and localized strengthening. The second factor is the entanglement of external dislocations in the α matrix. These dislocations, generated during FSP, develop over a longer period than those in the shear band. As shown in Fig. 4, the dislocation network, localized and separated from the shear band by stacking faults, also contributes to strengthening. Fig. 12 illustrates the movement and absorption of dislocations near the shear band. Additionally, shear bands based on α twins (Fig. 8) positively influence strengthening, as tiny twins on the shear band boundary obstruct and absorb dislocations.

Due to the sluggish diffusion of high-entropy components, the shear band's substructure remains relatively stable, with its formation determined by the FSP rotation speed. Consequently, specimen 375 exhibits higher hardness and modulus than specimen 225. During subsequent heat treatment, pre-existing defects begin to recover and disappear, though recovery is asynchronous. Dislocations and thin stacking faults in the α matrix recover quickly, whereas the shear band and surrounding regions experience more difficult recovery. The mixed α and bcc phases at the shear band boundary suppress dislocation migration as temperature increases. The bcc twin, shear band boundary, and connected stacking fault together form a defect lock, prolonging the lifespan of the region affected by the shear band. Short heat treatment facilitates the complete diffusion of high-entropy components and shear band formation, mitigating the softening effect of recovery and resulting in high hardness and modulus values in specimen 225HT1. Over time, recovery becomes the main mechanism, leading to a marked reduction in hardness and modulus.

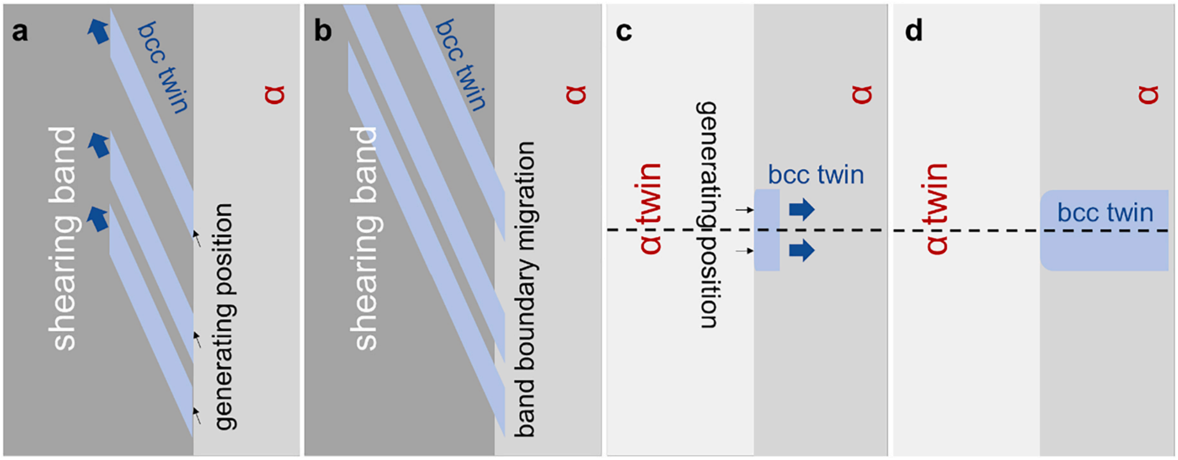

Fig. 11. Towing process in the shear band (a–b) away from the α twin; (c–d) near the α twin.

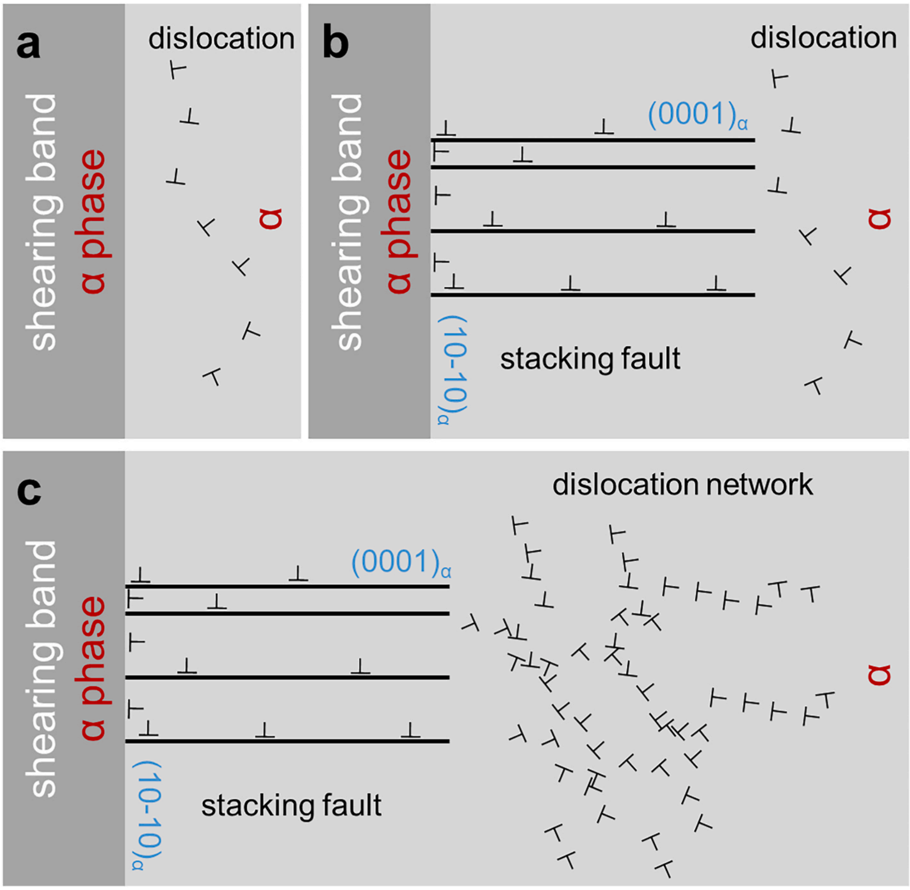

Fig. 12. Movement and absorption of dislocations near the shear band: (a) initial state; (b) formation of stacking faults; (c) formation of a dislocation network.

4.3.2. *Toughening effect of shear bands and stacking faults*

The potential for plastic deformation is enhanced following modification, with highly dispersed precipitation induced by shear bands playing a crucial role. Due to the small size of the shear band, the bcc phase generated inside the shear band does not aggregate into large particles, avoiding the distribution of incoherent particles on grain boundaries, which benefits the alloy's toughness [97].

As discussed, dislocations in both the shear band and the surrounding α matrix have difficulty moving to the intermediate region (Fig. 4). Additionally, no heterogeneous nucleation sites are produced (Fig. 6), resulting in a relatively low density of dislocations between stacking faults. According to R. Liu et al., dislocations can traverse thin stacking faults before narrowly spaced stacking fault networks form [98]. Therefore, the intermediate region tends to promote plastic deformation early on, inducing a hardening effect after significant dislocation stacking, further enhancing toughness.

4.3.3. *Suppressing effect of shear bands on martensitic transformation*

Notably, martensite, typically induced by severe deformation in the TC4 alloy, is not detected in specimen 375. High-entropy stripes occupy a large area in the stir zone, making the region affected by shear bands influential on martensitic transformation. Dislocations in the α matrix are primarily obstructed, making it difficult for particles to migrate to the β phase post-shear band formation. Dislocations in the β phase are mainly absorbed by the β twin at the shear band's end, preventing dislocation aggregation in the β phase away from the shear band. Consequently, stress remains relatively low, restricting martensite induction. During subsequent heat treatment, although the shear band-affected region gradually reduces, martensite formation remains challenging due to the absence of deformation. In specimens processed at a lower rotation rate (225 rpm) with incomplete diffusion, the large area affected by the shear band continues to suppress martensitic transformation. Thus, the impact of rotation rate and heat treatment on martensite formation is negligible, corresponding to similar superelasticity results across specimens with varying rotation rates and heat treatments.

5. Conclusion

In this study, the high entropy element introduced by FSP significantly improves the surface properties of Ti6Al4V alloy, which has important practical application value for aerospace, biomedical implants and extreme environment engineering. Especially in the biomedical field, the modified alloy exhibits excellent superelasticity and stability, which helps to improve the long-term service performance and biocompatibility of the implant. The FSP technology is not only suitable for Ti6Al4V alloy, but also can be extended to the surface modification of other metal materials, such as titanium alloy, magnesium alloy, etc., to meet the needs of different engineering applications.

In summary, equiatomic TiNbHfZnZr high-entropy components were introduced to reinforce Ti6Al4V alloy via friction stir processing. The formation of shear bands and their effects on the surrounding microstructure and mechanical properties were analyzed. The main findings are as follows.

1. With the dilution of the α matrix, the atomic size mismatch of high-entropy components remains relatively high, allowing the dual-phase structure to be largely retained and stabilizing the shear band.
2. Shear bands induced by high-entropy components form within the α matrix and subsequently develop into the (α+bcc) sub-microstructure. Due to low surface energy, $(0001)_{\alpha}$ stacking faults perpendicular to the shear band boundary create a unidirectional dislocation region, while bcc twins generated at the shear band boundary grow at an angle of 33° to the shear band boundary.
3. The absorption of dislocations leads to the generation of β twins within the β lath, which serve as the termination points of the shear bands. Consequently, the length of the shear band is determined by the β lath. In contrast, the movement of dislocations within the α matrix is blocked by stacking faults, resulting in the entanglement and formation of dislocation networks. The development of stacking faults is thereby suppressed and eventually halted.
4. The α twin also influences the formation of shear bands. As the bcc twinning process progresses, high-entropy components tend to diffuse along the initial α twin boundary, forming a bcc lattice. Thus, a bcc twin connected by an α twin presents a complete lath rather than several needles.
5. The bcc twin, shear band boundary, associated stacking faults, and dislocation network collectively contribute to a strengthening effect. The modification by high-entropy components enhances both the modulus and hardness. Additionally, the extensive region influenced by shear bands suppresses martensitic transformation, leading to the stable superelasticity of the modified alloy.

Declaration of competing interest

The authors declare that they have no known competing financial interests or personal relationships that could have appeared to influence the work reported in this paper.

Acknowledgements

The authors would like to acknowledge the financial supports of National Natural Science Foundation of China under Grant No.52274387, 52311530772. Thanks for the Guangxi Key Laboratory of Basic and Translational Research of Bone and Joint Degenerative Diseases (21-220-06).

References

[1] Zhang T, Wei D, Lu E, Wang W, Wang K, Li X, Zhang L, Kato H, Lu W, Wang L. J Mater Sci Technol 2022;131:68.
[2] Zhang Y, Liu J, Wang L, Wei D, Liu C, Wang K, Tang Y, Zhang L, Lu S, Wang L. Acta Mater 2022;239:118295.
[3] Cui Y, Chen L, Chu Y, Zhang L, Li R, Lu S, Wang L, Zhang L. Corrosion Sci 2023;215:111017.
[4] Guo L, Naghavi SA, Wang Z, Varma SN, Han Z, Yao Z, Wang L, Wang L, Liu C. Mater Des 2022;216:110552.
[5] Cui Y, Chen L, Qin P, Li R, Zang Q, Peng J, Zhang L, Lu S, Wang L, Zhang L. Corrosion Sci 2022;203:110333.
[6] Zhang J, Bermingham M, Otte J, Liu Y, Dargusch M. Scripta Mater 2023;223:115066.
[7] Poulain R, Amann F, Deya J, Bourgon J, Delannoy S, Prima F. Mater Lett 2022;317:132114.
[8] Hu S, Li T, Su Z, Liu D. Intermetallics 2022;140:107401.
[9] Liu C, Xie L, Zhang LC, Wang L. Materials Research Letters 2024;12:425.
[10] Cui YW, Wang L, Zhang LC. Prog Mater Sci 2024;144:101277.
[11] Rogl G, Ghosh S, Wang L, Bursik J, Grytsiv A, Kerber M, Bauer E, Mallik RC, Chen X, Zehetbauer M, Rogl P. Acta Mater 2020;183:285.
[12] Verma N, Pant N, Beach JA, Ivanisenko Y, Ashkenazy S, Dillon S, Bellon P, Averback RS. Acta Mater 2019;170:218.
[13] Wang C, Yu D, Niu Z, Zhou W, Chen G, Li Z, Fu X. Acta Mater 2020;200:101.
[14] Yang C, Li MQ, Liu YG. J Alloys Compd 2021;854:157277.
[15] Qiao K, Zhang T, Wang K, Yuan S, Wang L, Chen S, Wang Y, Xue K, Wang W. J Mater Res Technol 2022;18:1166.
[16] Zhou X, He L, Zhang M, Wang P. Optik 2023;285:170987.
[17] Ma Q, Zhao W, Shi C, Wang M, Song C, Zhang H, Gao S. Mater Char 2023;205:113300.
[18] Wang L, Xie L, Lv Y, Zhang L, Chen L, Meng Q, Qu J, Zhang D, Lu W, Hua L. Acta Mater 2017;131:499.
[19] Wang L, Xie L, Shen P, Fan Q, Wang K, Lu W, Hua L, Zhang L. Mater Char 2019;153:175.
[20] Wang L, Wang Y, Huang W, Liu J, Tang Y, Zhang L, Fu Y, Zhang L, Lu W. Mater Des 2020;194:108961.
[21] Fang Y, Wang Q, Yang Z, Wang W, Liu J, Ma J, Fu Y. Mater Des 2022;221:110987.
[22] Zhang C, Ding Z, Xie L, Zhang L, Wu L, Fu Y, Wang L, Lu W. Appl Surf Sci 2017;423:331.
[23] Xie L, Wang L, Wang K, Yin G, Fu Y, Zhang D, Lu W, Hua L, Zhang L. Materialia 2018;3:139.
[24] Jiang PF, Li XR, Zong XM, Wang XB, Chen ZK, Liu CZ, Gao NK, Zhang ZH. J Alloys Compd 2022;926:166813.
[25] Yin Y, Kou W, Zhao Y, Yang H, Zeng W. Scripta Mater 2022;219:114854.
[26] Yang ZW, Fu LQ, Wang SL, Zhang M, Wang Y, Ma ZQ, Wang DP. Addit Manuf 2021;39:101883.
[27] Jian S, Wang J, Xu D, Ma R, Huang C, Lei M, Liu D, Wan M. Mater Des 2022;222:111031.
[28] Davids WJ, Chen H, Nomoto K, Wang H, Babu S, Primig S, Liao X, Breen A, Ringer SP. Acta Mater 2021;215:117131.
[29] Wang H, Zhang HM, Cheng XW, Mu XN. Mater Sci Eng, A 2022:144240. in press.
[30] Lu Q, Lv Y, Zhang C, Zhang H, Chen W, Xu Z, Feng P, Fan J. J Mater Sci Technol 2022;110:24.
[31] Ma ZY, Mishra RS, Tjong SC. Acta Mater 2002;50:4293.
[32] Liu S, Han S, Zhang L, Chen L, Wang L, Zhang L, Tang Y, Liu J, Tang H, Zhang L. Compos B Eng 2020;200:108358.
[33] Deore HA, Nichul U, Rao AG, Hiwarkar VD. Surf Coating Technol 2022;449:128985.
[34] Gu H, Ding Z, Yang Z, Yu W, Zhang W, Lu W, Wang L, Fu Y. Mater Des 2019;169:107680.
[35] Zhang Y, Wei D, Chen Y, Xie L, Wang L, Zhang LC, Lu W, Chen G. J Mater Sci Technol 2024;186:48.
[36] Zhang Y, Wang L, Lan C, Wei D, Chen Y, Xie L, Zhang L, Lu W, Chen G. Mater Des 2024;243:113049.
[37] Wang Y, Wei D, Wang L, Zhang L, Liu J, Tang Y, Fu Y, Lu W. Appl Surf Sci 2022;583:152495.
[38] Wang Y, Shi H, Zhou P, Tang Y, Liu J, Wang L, Li J, Fu Y, Lu W. J Mater Res Technol 2021;15:6442.
[39] Kolli SK, Natarajan AR, Ven AV. Acta Mater 2021;221:117429.
[40] Pandey P, Makineni SK, Samanta A, Sharma A, Das SM, Nithin B, Srivastava C, Singh AK, Raabe D, Gault B, Chattopadhyay K. Acta Mater 2019;163:140.
[41] Paul A, Kodentsov AA, Loo FJJ. Acta Mater 2004;52:4041.
[42] Ren X, Hagiwara M. Acta Mater 2001;49:3971.
[43] Tsai KY, Tsai MH, Yeh JW. Acta Mater 2013;61:4887.

[44] Qin G, Chen R, Mao H, Yan Y, Li X, Schonecker S. Vito. Acta Mater 2021;208:116763.
[45] Jiang D, Xie L, Wang L. J Mater Res Technol 2023;26:1341.
[46] Jiang D, Li Y, Wang L, Zhang L-C. Small Structures. In Press; 2024, 2400110.
[47] Cantor B, Chang ITH, Knight P, Vincent AJB. Mater Sci Eng, A 2004;375–377:213.
[48] Yeh JW, Chen SK, Lin SJ, Gan JY, Chin TS, Shun TT, Tsau CH, Chang SY. Adv Eng Mater 2004;6:299.
[49] Li T, Wang S, Fan W, Lu Y, Wang T, Li T, Liaw PK. Acta Mater 2023;246:118728.
[50] Chen S, Ma Z, Qiu S, Zhang L, Zhang S, Yang R, Hu Q. Acta Mater 2022;225:117582.
[51] Jiang L, Hu Y, Sun K, Xiu P, Song M, Zhang Y, Boldman WL, Crespillo ML, Rack PD, Qi L, Weber WJ, Wang L. Adv Mater 2020;32:2002652.
[52] Liu C, Gadelmeier C, Lu S, Yeh J, Yen H, Gorsse S, Glatzel U. Acta Mater 2022;237:118188.
[53] Calin M, Vishnu J, Thirathipviwat P, Popa M-M, Krautz M, Manivasagam G, Gebert A. Mater Sci Eng C 2021;121:111733.
[54] Liu C, Wang Y, Zhang Y, Wang L. Acta Metall Sin 2024;37:3.
[55] Liu C, Wang Y, Zhang Y, Zhang LC, Wang L. Int J Plast 2024;173:103884.
[56] Kim JH, Hidayati R, Jung S, Salawu YA, Kim H, Yun JH, Rhyee J. Acta Mater 2022;232:117971.
[57] Moore CM, Wilson JA, Rushton MJD, Lee WE, Astbury JO, Middleburgh SC. Acta Mater 2022;229:117832.
[58] Wang Y, Zhang Y, Wang L, Liu J, Tang Y, Ma X, Lu W. J Mater Res Technol 2023;24:8940.
[59] Wang Y, Wei D, Wang L, Zhang L, Liu J, Tang Y, Fu Y, Lu W. Appl Surf Sci 2022;583:152495.
[60] Wang Y, Shi H, Zhou P, Tang Y, Liu J, Wang L, Li J, Fu Y, Lu W. J Mater Res Technol 2021;15:6442.
[61] Lv Y, Ding Y, Han Y, Zhang L, Wang L, Lu W. Mater Sci Eng, A 2017;685:439.
[62] Gangwar K, Ramulu M. Mater Des 2018;141:230.
[63] Zhao B, Lv Y, Ding Y, Wang L, Lu W. Mater Char 2018;144:77.
[64] Santos R, Rossi M, Vidilli A, Borras V, Afonso C. J Mater Res Technol 2023;22:3511.
[65] Paul M, Yang F, Bolzoni L. Mater Sci Eng, A 2023;866:144675.
[66] Rogal L, Ikeda Y, Lai M, Körmann F, Kalinowska A, Grabowski B. Mater Des 2020;192:108716.
[67] Nagase T, Todai M, Nakano T. Scripta Mater 2020;186:242.
[68] Li T, Chen H, Zhou Z, Li S, Wang Y. Intermetallics 2023;152:107753.
[69] Kubilay RE, Curtin WA. Acta Mater 2021;216:117119.
[70] Li Z, Kormann F, Grabowski B, Neugebauer J, Raabe D. Acta Mater 2017;136:262.
[71] Ren L, Xiao W, Kent D, Wan M, Ma C, Zhou L. Scripta Mater 2020;184:6.
[72] Yang R, Yang L, Wang T, Wang Q. Mater Sci Eng, A 2023;870:144880.
[73] Li X, Zhao Q, Tian Y, Wang Q, Fan J, Song K, Zhou H, Wang J. Acta Mater 2023;249:118815.
[74] Zahiri A, Vitral E, Ombogo J, Lotfpour M, Cao L. Acta Mater 2023;241:118377.
[75] Pantawane MV, Yang T, Jin Y, Mazumder S, Pole M, Dasari S, Krokhin A, Neogi A, Mukherjee S, Banerjee R, Dahotre NB. Mater Sci Eng, A 2021;811:140990.
[76] Yuan L, Xiong J, Du Y, Wang Y, Shi J, Li J. J Alloys Compd 2018;763:376.
[77] Wang M, Huang H, Wen M, Fan F. Mater Sci Eng, A 2020;788:139602.
[78] Mater Lett 2019;242:123.
[79] Rashid S, Vita GM, Persichetti L, Lucci G, Battocchio C, Daniel R, Visaggio D, Marsotto M, Visca P, Bemporad E, Capellini G, Sebastini M, Masi A. Appl Surf Sci 2022;573:151604.
[80] Liu J, Scales R, Li B, Goode M, Young B, Hu J, Wilkinson A, Armstrong D. J Alloys Compd 2023;932:167651.
[81] Zarei Z, Zohevand M, Momeni A, Sadeghpour S, Somani M. J Alloys Compd 2023:169818. *in press*.
[82] Kovacocy P, Simekova B, Kovarikova I, Hodulova E, Domankova M, Ptacinova P, Jurci P. J Mater Eng Perform 2020;29:593.
[83] Zhang J, Cui D, Li X, He Y, Wang H, Liu W. J Mater Sci Technol 2023;156:92.
[84] Guo S, Liu CT. Prog Nat Sci: Mater Int 2011;21:433.
[85] Chanda B, Das J. J Alloys Compd 2019;798:167.
[86] Zhang Y, Zhou Y, Lin J, Chen G, Liaw P. Adv Eng Mater 2008;10:534.
[87] Zhang S, Ding X, Gao X, Chen R, Cao W, Su Y, Guo J. Int J Plast 2023;160:103505.
[88] Zhang J, Gadelmeier C, Sen S, Wang R, Zhang X, Zhong Y, Glatzel U, Grabowski B, Wilde G, Divinski S. Acta Mater 2022;233:117970.
[89] Liu X, Yin X, Yang X, Chen H, Wang J. Scripta Mater 2022;221:114957.
[90] Zhan H, Wang G, Kent D, Dargusch M. Acta Mater 2016;105:104.
[91] Berg L, Gjønnes J, Hansen V, Li X, Wedel M, Waterloo G, Schryvers D, Wallenberg L. Acta Mater 2001;49:3443.
[92] Rosner H, Schloßmacher P, Shelyakov A, Glezer A. Acta Mater 2001;49:1541.
[93] Wei B, Wu W, Gong M, Yu S, Ni S, Song M, Wang J. Acta Mater 2023;245:118637.
[94] Mu Y, He L, Deng S, Jia Y, Jia Y, Wang G, Zhai Q, Liaw P, Liu C. Acta Mater 2022;232:117975.
[95] Li Z, Zhao S, Alotaibi S, Liu Y, Wang B, Meyers M. Acta Mater 2018;151:424.
[96] Otto F, Dlouhy A, Somsen C, Bei H, Eggeler G, George E. Acta Mater 2013;61:5743.
[97] Jang T, Choi W, Kim D, Choi G, Jun H, Ferrari A, Kormann F, Choi P, Sohn S. Nat Commun 2021;12:4703.
[98] Liu R, Tang J, Jiang J, Li X, Wei Y. Extreme Mechanics Letters 2022;56:1201875.